Insights into the Preparation of Copper Catalysts Supported on Layered Double Hydroxide Derived Mixed Oxides for Ethanol Dehydrogenation

Rodrigo M M Santos, Valérie Briois, Leandro Martins, Celso V Santilli

Insights into the Preparation of Copper Catalysts Supported on LDH-Derived Mixed Oxides for Ethanol Dehydrogenation

Rodrigo M. M. Santos,[†,‡,] Valérie Briois,[‡] Leandro Martins,[†] and Celso V. Santilli[†,]**

[†]São Paulo State University (UNESP), Institute of Chemistry, Rua Prof. Francisco Degni 55, 14800-060, Araraquara, SP, Brazil

[‡]SOLEIL Synchrotron, L'Orme des Merisiers, BP48, Saint-Aubin, 91192, Gif-sur-Yvette, France

*rodrigo.morais@unesp.br (R.M.M. Santos) and cv.santilli@unesp.br (C.V. Santilli).

KEYWORDS: Layered double hydroxide (LDH), copper-based catalyst, ethanol dehydrogenation reaction (EDR), acetaldehyde, *operando* quick-EXAFS.

ABSTRACT: Acetaldehyde is an important chemical commodity and a building block for producing several other high-value products in the chemical industry. This has motivated the search for suitable efficient, stable, and selective catalysts, as well as renewable raw materials, such as ethanol. In this work, supported copper catalysts were prepared from CuZnAl layered double hydroxides (LDH) with different copper contents (5, 10, and 20 wt.%), for application in the ethanol dehydrogenation reaction (EDR). The samples were thoroughly characterized by a series of techniques, which allowed analysis of all the copper and zinc species involved in the

different catalyst preparation steps and during the EDR. The results obtained by *in situ* quick-EXAFS measurements, combined with multivariate data analysis, showed that the copper content in the pristine LDH influenced the phase composition of the mixed oxide support, which consequently affected the dispersion of copper nanoparticles. The higher the copper content, the higher the $ZnAl_2O_4$ and zinc tetrahedral pre-nuclei (TPN) contents, to the detriment of the ZnO content. All the samples showed high selectivity (>97%) and stability in the catalytic reactions at 300 and 350 °C, with no observed deactivation during 6 h on-stream. Although the samples with lower copper content presented higher copper dispersion and reactivity, the sample containing 20 wt.% of copper outperformed the others, with greater conversion and higher activity towards acetaldehyde.

1. INTRODUCTION

Acetaldehyde is an important chemical used as an additive in the food industry and as a platform molecule in organic syntheses to produce amino acids, pyridines, ethyl acetate, and other substances.[1] Acetaldehyde production is estimated to exceed 1.4 million tons by 2022,[2] mainly obtained by ethylene oxidation. However, renewable raw materials have been sought as alternative feedstocks,[3, 4] such as in the ethanol dehydrogenation reaction (EDR):[5]

$$CH_3CH_2OH \rightleftharpoons CH_3CHO + H_2$$

Supported Cu catalysts are very active for the EDR, producing hydrogen and acetaldehyde as the main products when the reaction is carried out at atmospheric pressure.[6] However, the design of catalysts with high selectivity towards acetaldehyde, together with high ethanol conversion, is a matter of ongoing research, since high conversion usually gives rise to the formation of many other products, mainly resulting from the coupling of ethanol with acetaldehyde and leading to the formation of ethyl acetate.[7]

The dispersion of copper on the catalyst plays a vital role in determining the catalytic activity towards acetaldehyde formation.[8] In recent work by our group, it was found that the EDR reaction carried out using copper supported on hierarchically porous alumina (Cu/Al_2O_3) could convert more than 80% of ethanol at 300 °C, with selectivity to acetaldehyde higher than 80% and activity strongly dependent on the Cu loading and dispersion.[4] Sintering of copper nanoparticles is often reported as the primary deactivation process of EDR catalysts, due to the use of temperatures ranging between the Hüttig (174 °C) and Tamman (405 °C) temperatures of metallic copper.[9] To overcome the mobility of copper atoms at the catalyst surface leading to nanoparticle sintering, metal oxides irreducible under dehydrogenation conditions are added during catalyst preparation, as either supports or promoters.[6, 10] The choice of the metal oxide is crucial for the final selectivity of the catalyst, since the coupling of ethanol with acetaldehyde, giving rise to byproducts, is the result of reactions taking place at the metal oxide surface, rather than at the copper nanoparticle surface.[7] For decades, supports based on ZnO[11] or a ZnO/Al_2O_3 mixture[6] have been commonly used for the preparation of copper catalysts employed in the EDR. The presence of ZnO, mainly in nanometric sizes, strengthens the interfacial contact with Cu by means of epitaxial or electronic bonding.[12, 13] This intimate contact promotes a more efficient dispersion of the active phase, improving catalytic performance and providing stabilization against sintering.[12] High selectivity of Cu/ZnO-based catalysts towards acetaldehyde formation (~90%) is mainly reported for temperatures ≤200 °C, but with quite low ethanol conversion (≤20%)[14] or rapid deactivation as a function of time on-stream, as observed for an industrial $CuO/ZnO/Al_2O_3$ catalyst operating at atmospheric pressure.[6] $ZnAl_2O_4$ has also been recently reported as a support for copper, showing excellent selectivity towards acetaldehyde (>95%) at low ethanol conversion (12% at 250 °C) and achieving 90% selectivity at total ethanol conversion (400 °C).[1] In this study, it was suggested that

the dispersion of copper achieved on the $ZnAl_2O_4$ was able to poison the dehydration activity of the spinel, reducing to zero its activity in producing diethyl ether and ethylene at low temperatures. These studies indicate that the copper loading and the size and dispersion of active species are key parameters for tuning in order to achieve high selectivity towards different products. The characteristics of the support, together with its ability to stabilize the dispersion of copper nanoparticles, are also important features to control.

Layered double hydroxides (LDH) and their thermally decomposed derivatives have received much attention in the past decades, due to critical practical applications including their use as adsorbents,[15] ion exchangers,[16] and catalysts.[17] LDH are described by the formula $[M^{2+}_{(1-x)}M^{3+}_x(OH)_2\ A^{n-}_{x/n}\cdot zH_2O]$, where M^{2+} and M^{3+} are metal cations occupying the octahedral interstices of the inorganic layers, and A^{n-} represents intercalated anions. In addition to broad flexibility in selection of the M^{2+} and M^{3+} composition, including the ability to use several transition metals (such as Cr, Mn, Fe, Co, Ni, Cu, and Zn), LDH are desirable in catalysis due to the uniform distribution of metal cations at an atomic level within the layers.[18] LDH have been used as functional supports following the partial substitution of some metal cations by catalytically active species.[18] Mild thermal treatment (400-500 °C), with activation under appropriate conditions, has been used to prepare metallic nanoparticles supported in a mixed oxide matrix ($M^{2+}O$, $M^{3+}{}_2O_3$, and $M^{2+}M^{3+}{}_2O_4$).[19] This method is advantageous, compared to the traditional route of incipient wetness impregnation, since it generates well-dispersed metallic nanoparticles with uniform sizes, while providing good thermal stability.[18] An inhomogeneous distribution of active species weakly interacting with the support can favor particle sintering, causing catalyst deactivation. For instance, in a recent study using Cu-impregnated MgAl mixed oxides as catalyst precursors for the EDR,[17] the reference non-porous catalyst was substantially deactivated (21.1%

after 6 h at 300 °C) due to copper particles sintering. In contrast, deactivation of around 8.2% was observed for a macro-mesoporous support,[17] emphasizing the importance of catalyst design and synthesis method for ensuring high dispersion and stability.

Time-resolved X-ray absorption spectroscopy (quick-XAS), together with multivariate data analysis based on principal component analysis (PCA) and multivariate curve resolution with alternating least squares (MCR-ALS) fitting, have become powerful tools for the *operando* monitoring of catalyst activation and reaction.[20-22] These techniques have been applied to elucidate the behaviors of different species formed during catalyst processing and use, even when such species have neither long-range order nor suitable references for the purpose of comparison. A recent *in situ* quick-EXAFS investigation of poly(methyl methacrylate) (PMMA)-embedded ZnAl, ZnCuAl, and ZnAlFe LDH samples[23] evidenced the involvement of three zinc-based species during the thermal decomposition of PMMA-LDH at moderate temperature (≤450 °C). It was found that the LDH was firstly transformed into an intermediate Zn-based spinel pre-nucleus (SPN), at around 180 °C, which was further converted to nanometric ZnO and $ZnAl_2O_4$ phases at higher temperatures. For this particular environment (LDH embedded in a polymeric matrix), the so-called SPN component was readily isolated from the XAS dataset. The existence of the SPN component raises questions concerning its presence in an LDH-derived catalyst, even in the absence of a polymeric matrix, and its possible effects on the properties of the final catalyst. The presence of ZnO and $ZnAl_2O_4$ as thermal decomposition products also requires detailed evaluation, in order to elucidate their effects on catalytic activity and selectivity.

Therefore, this work investigates the thermal decomposition of LDH, using CuZnAl-LDH precursors and performing an in-depth characterization of all the species present during the catalyst transformations. A detailed *operando* quick-EXAFS study coupled with multivariate data analysis

was applied to the main steps of catalyst processing and use in the EDR. Tailored catalysts were obtained by varying the Cu/Zn ratio, in order to achieve greater phase dispersion, high catalyst stability, and selectivity towards the formation of acetaldehyde.

2. EXPERIMENTAL

2.1. Catalysts preparation

2.1.1. LDH synthesis

Carbonate-intercalated CuZnAl-LDH samples were synthesized using a co-precipitation method at room temperature (RT, ~25 °C), as reported previously,[15] with a 2:1 of the M^{2+}:M^{3+} molar ratio. The salts used for the synthesis were $Cu(NO_3)_2 \cdot 2.5H_2O$ (Sigma-Aldrich, 98%), $Zn(NO_3)_2 \cdot 6H_2O$ (Sigma-Aldrich, 98%), $Al(NO_3)_3 \cdot 9H_2O$ (Sigma-Aldrich, ≥98%), and Na_2CO_3 (Sigma-Aldrich, ≥99.5%). The Cu/Zn ratio was adjusted to obtain 0, 5, 10, and 20 wt.% of Cu in the final catalyst (considering $Cu/ZnO/Al_2O_3$). The as-prepared samples were denoted "C", followed by their Cu loadings (i.e., C0-LDH, C5-LDH, C10-LDH, and C20-LDH). The experimental compositions of the LDH samples, obtained by inductively coupled plasma optical emission spectrometry (ICP-OES), are presented below. For each sample, the amount of water was calculated from the weight loss of the interlayer water, obtained from the thermogravimetry results.

$$C0\text{-}LDH = Cu_{0.000}Zn_{0.696}Al_{0.304}(OH)_{2.0}\,(CO_3)_{0.15} \cdot 0.63H_2O$$

$$C5\text{-}LDH = Cu_{0.056}Zn_{0.634}Al_{0.310}(OH)_{2.0}\,(CO_3)_{0.15} \cdot 0.65H_2O$$

$$C10\text{-}LDH = Cu_{0.102}Zn_{0.619}Al_{0.279}(OH)_{2.0}\,(CO_3)_{0.14} \cdot 0.58H_2O$$

$$C20\text{-}LDH = Cu_{0.220}Zn_{0.477}Al_{0.303}(OH)_{2.0}\,(CO_3)_{0.15} \cdot 0.57H_2O$$

2.1.2. Mixed metal oxides

To obtain the mixed oxides (MO) of the metal components, the as-prepared LDH samples were thermally decomposed by heating to 450 °C (at 5 °C min^{-1}) in an air atmosphere (30 mL·min^{-1}), maintaining the final temperature for 30 min. The MO samples were denoted C0-MO, C5-MO, C10-MO, and C20-MO.

2.1.3. Cu-impregnated samples

The LDH-derived catalysts were compared with two reference samples (IMP-LDH and IMP-REF) impregnated with 20 wt.% copper. The IMP-LDH was prepared from C0-LDH sample and IMP-REF sample was prepared with 1.49 mmol of ZnO (Synth, 99%) and 1.64 mmol of Al_2O_3 (APC-3017, Alcoa). The copper impregnation was made with 50 mL of an aqueous solution containing 1.13 mmol of $Cu(NO_3)_2 \cdot 2.5H_2O$ (Sigma-Aldrich, 98%). The mixture was subjected to rotary evaporation at 50 °C, under reduced pressure. After impregnation, the samples were calcined by heating to 450 °C, under a 30 mL·min^{-1} flow of air, maintaining the final temperature for 30 min.

2.2. Characterization methods

2.2.1. Conventional techniques

X-ray diffraction (XRD) patterns of the samples were recorded using a D2 PHASER (Bruker) X-ray diffractometer operating with Cu K_α radiation (λ = 0.154 nm). Thermogravimetric analysis and differential scanning calorimetry (TGA and DSC) were performed using a LABSYS evo STA 1600 (Setaram) instrument, with heating from RT to 450 °C, at 5 °C min^{-1}, under a flow of air at 30 mL min^{-1}, maintaining the final temperature for 30 min.

Specific surface area and mesoporosity determinations employed N_2 adsorption/desorption isotherms acquired with an ASAP2010 system (Micromeritics). Before each measurement, the sample was degassed at 200 °C for 12 h. The surface area was calculated using the Brunauer-Emmett-Teller (BET) model,[24] while the mesopore size distribution was obtained by the Barrett-Joyner-Halenda (BJH) method.[25]

Transmission electron microscopy (STEM) micrographs were acquired using an FEI Tecnai G2 F20 microscope operated at 200 kV and equipped with an energy dispersive X-ray (EDX) detector. For the analysis, the samples were suspended in isopropanol, dripped onto carbon-coated nickel grids, and dried in air.

2.2.2. Catalytic properties

Catalyst activity was analyzed using a micro activity reference system (PID Eng&Tech) operating in continuous flow mode at atmospheric pressure. The catalyst performance was first evaluated for 45 min at 220, 250, 300, and 350 °C. Considering the temperatures at which the best performances were achieved, catalyst stability was investigated by monitoring of the EDR for 6 h at 300 and 350 °C. The reactor and valves inside the hot box were kept heated at 180 °C to avoid condensation of reactants and products. A fixed bed reactor was used to perform the reduction and EDR reactions. A 100 mg mass of powdered MO was heated from RT to 350 °C, in a 30 mL min^{-1} N_2 flow, and was then reduced *in situ* at 350 °C for 15 min, in a 30 mL min^{-1} flow of diluted H_2 (5% v/v in N_2). The reactor was fed with 0.1 mL min^{-1} of pure ethanol (99.8 wt.%) supplied using an HPLC pump (Model 307, Gilson) and transported in a 30 mL min^{-1} flow of N_2. These conditions resulted in a weight hourly space velocity (WHSV) of 47.3 h^{-1}. The products in the outlet stream were analyzed on-line using a gas chromatograph (Model 2014, Shimadzu) equipped with a flame ionization detector and an Rtx-1 capillary column (30 m x 0.32 mm i.d.; 1 μm film

thickness). The ethanol conversion (χ_{EtOH}), selectivity (S_i), and turnover frequency (TOF) were calculated according to Equations 1, 2, and 3, respectively.

$$\chi_{\mathrm{EtOH}}(\%) = \frac{F_{in} - F_{out}}{F_{in}} \cdot 100 \quad (1)$$

$$S_i(\%) = \frac{nC_i \cdot F_i}{\sum_{i=1}^{N} nC_i \cdot F_i} \cdot 100 \quad (2)$$

$$TOF(s^{-1}) = \frac{mol\ of\ converted\ ethanol}{mol\ of\ surface\ copper\ atoms \cdot time} \quad (3)$$

where, F_{in} and F_{out} are the molar flows of ethanol in the inlet and outlet streams (mol min^{-1}), respectively, and nC_i and F_i (mol min^{-1}) are the carbon amount and the molar outflow of product i.

2.2.3. Advanced synchrotron radiation-based techniques

The LDH long-range order was investigated *in situ* by XRD during CuZnAl-LDH thermal decomposition and catalyst activation (MO reduction). The measurements were performed at the XPD beamline of the Brazilian synchrotron radiation facility (LNLS), which was equipped with a Si(111) monochromator and operated at 8 keV (λ = 0.155 nm), with a step size of 0.003° and 2 s exposure time. For the experiments, the samples were loaded into a homemade oven and diffractograms were collected in a limited 2θ range between 21 and 51°, in order to improve the temporal resolution.

Characterization by XAS was carried out at the ROCK quick-EXAFS beamline[26] of the French SOLEIL synchrotron radiation facility. Spectra were acquired simultaneously at the Cu (8979 eV) and Zn (9659 eV) K-edges during thermal decomposition, catalyst activation, and *operando* EDR. The Si(111) channel-cut oscillation frequency was set to 2 Hz, recording two quick-EXAFS spectra, every 0.5 s. Every 10 acquired spectra were

merged, in order to improve the signal/noise ratio. The quick-EXAFS measurements were performed simultaneously with the analysis of gas phase composition using a coupled on-line mass spectrometer (MS) (Cirrus LM99, MKS). Energy calibration and a raw XAS data normalization procedure were first carried out using a Python GUI developed at the ROCK beamline.[27] The normalized XAS dataset was analyzed by PCA and MCR-ALS,[28] using the free MCR-ALS GUI 2.0 toolbox, on the Matlab® platform.[29] The MCR-ALS procedure applied to XAS spectral data acquired during monitoring of a reaction enables the isolation of pure species involved in the reaction and observation of the evolution of their concentrations during the process. Further details about the MCR-ALS method applied to XAS are available in recent publications.[20, 30-32]

Structural parameters of the samples were obtained by least squares fitting of the Fourier transformed $k^2\chi(k)$ EXAFS data, using Artemis graphical interface software.[33] To fit the EXAFS data, values of E_0 (used for k-scaling) and S_0^2 (the amplitude reduction factor) were obtained by fitting the EXAFS spectra of bulk references (CuO, Cu_2O, and Cu). For the activated samples, this enabled determination of the first nearest neighbor coordination numbers ($N_{Cu\text{-}Cu}$) and their distances ($R_{Cu\text{-}Cu}$). Considering all the copper atoms to be distributed as metallic nanoparticles in a cuboctahedral structure,[34] the apparent Cu^0 dispersion (D_{Cu}), metallic surface area (S_{Cu}), and nanoparticle size (d_{Cu}) were estimated based on the following relationships:[5, 34]

$$N_{Cu-Cu} = \frac{24L(5L^2 + 3L + 1)}{10L^3 + 15L^2 + 11L + 3} \quad (4)$$

$$D_{Cu}(\%) = \frac{30L^2 + 6}{10L^3 + 15L^2 + 11L + 3} \cdot 100 \quad (5)$$

$$S_{Cu}(\mathrm{m^2\ g^{-1}}) = 6.4955 \cdot 10^{-2} \cdot C_{Cu} \cdot D_{Cu} \quad (6)$$

$$d_{Cu}(\text{nm}) = \frac{600M}{D_{Cu}\rho\sigma N_0} \quad (7)$$

where, L is the cluster order parameter, C_{Cu} is the copper content in wt.%, M is the Cu molecular mass, ρ is the Cu metal density (8.94 g cm^{-3}), σ is the surface area per Cu atom (0.0685 nm^2 $atom^{-1}$), and N_0 is the Avogadro constant.

3. RESULTS AND DISCUSSION

3.1. Characteristics of the as-prepared LDH

The X-ray diffraction patterns of the as-prepared LDH (Figure S1a, Supplementary Information) displayed the (003) and (006) diffraction peaks related to the stacking planes of lamellae, together with other peaks characteristic of the LDH structure. The basal distances (d) and average crystallite sizes (D) were calculated using the Bragg ($n\lambda = 2d\sin\theta$) and Scherrer ($D = 0.9\lambda / \beta\cos\theta$) equations, based on the (003) and (006) peak positions (θ) and their full width at half-maximum (β). Irrespective of the LDH composition, the basal distance was 0.755 nm, in agreement with the value observed previously for carbonate-intercalated LDH.[15] Similarly, for all the samples, the average crystallite size in the *c* direction was almost invariant, at around 31 nm.

3.2. LDH-MO conversion

Figure 1 shows the TGA and DSC profiles of the LDH, together with the monitoring of the water and carbon dioxide mass signals (m/z = 18 and 44, respectively), under the same conditions. All the samples had similar TGA and DSC profiles, with two main endothermic events, reaching total weight losses of approximately 29%, which remained invariant during the isothermal step at 450 °C. Initially, at temperatures between RT and 120 °C, there was the removal of weakly

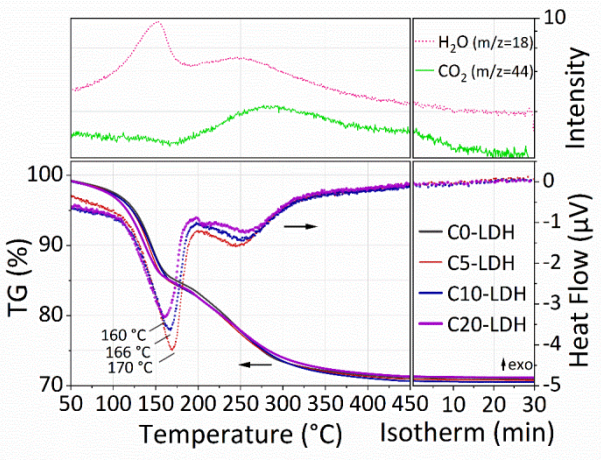

Figure. 1. TGA and DSC analysis under an air flow, together with monitoring of the water and carbonate mass signals. The mass signals are for the C10-LDH sample; all the other samples showed approximately the same profiles.

adsorbed water molecules. Intense heat absorption was observed between 120 and 200 °C, related to the removal of intercalated water, together with partial lamellae dehydroxylation, corresponding to the most intense water signal in the mass spectrum. This caused the collapse of the layered structure and formation of the mixed metal oxides. The last event was related to the decomposition of carbonate anions from the interlayer domain, concomitant with further lamellae dehydroxylation from 200 °C to around 450 °C. The decrease in temperature at the first endothermic peak revealed a weakening interaction, implying that the removal of water molecules and dehydroxylation became easier for the samples with greater Cu contents.[35] A similar effect was also reported for CuMgAl-LDH samples.[35] These findings could be explained by the Jahn-Teller distortion of divalent copper in octahedral coordination, lowering the stability of the lamellae when copper had substituted zinc.[36, 37]

The thermal decompositions of LDH to MO were monitored by *in situ* XRD (Figure 2). The progressive decrease in intensity of the LDH-related stacking peaks (006) and (009) was

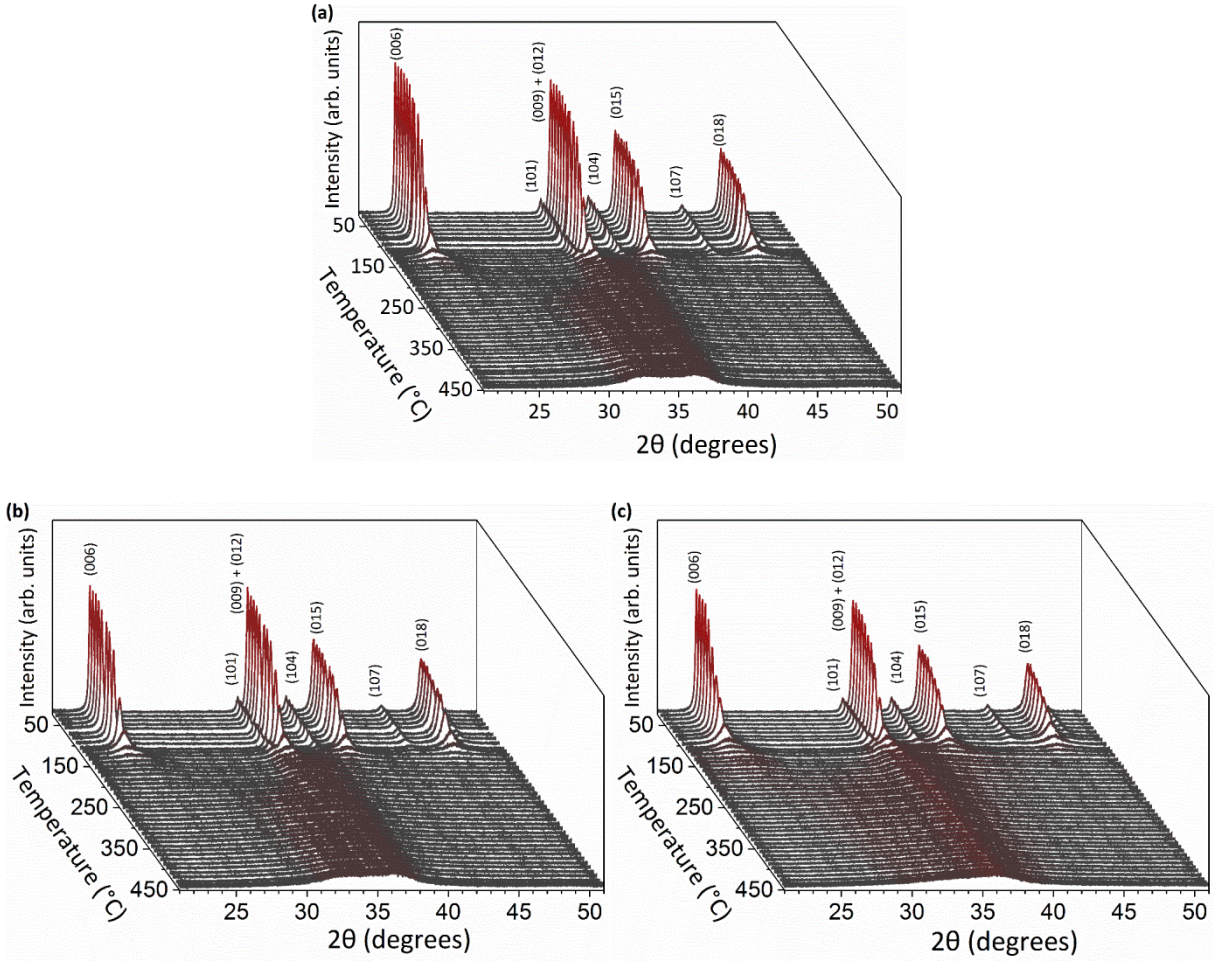

Figure 2. X-ray diffractograms collected *in situ* during the thermal decomposition of (a) C5-LDH, (b) C10-LDH, and (c) C20-LDH, with heating from RT to 450 °C.

accelerated above 100 °C, until their disappearance at around 200 °C. Above this temperature, the lamellar structure collapsed, with the appearance of broadened peaks with low intensity, consistent with the formation of nanocrystalline Zn, Al, and Cu-based oxide phases. The ZnO and CuO diffraction peaks were not easily separated (Figure S1b), due to the contribution of several factors, including dispersion of the homogeneous phase, low crystallinity, and the overlap of diffraction peaks associated with the oxidic phases. Nevertheless, it was evident that a higher copper content led to greater asymmetry between the (100) and (101) ZnO signals (Figure S1b), due to the increased intensity of the overlapped (002) and (111) CuO diffraction peaks in the same 2θ region.

The textural properties of the MO were evaluated using N_2 adsorption/desorption isotherms (Figure S2a). All the samples displayed type II isotherms, with a mixture of H1 and H3 hysteresis loops, characteristic of the coexistence of macropores and mesopores,[38] composed by tubular (H1) and slit-shaped pores (H3). The slit-shaped pores were formed by aggregation of the MO platelets, while the tubular structures were due to larger pores formed between compacted aggregates (Figure S3). It could be seen that the specific surface area decreased (91, 84, and 68 $m^2\ g^{-1}$) and that the mesopore volume increased (0.09, 0.10, and 0.13 $cm^3\ g^{-1}$), as the copper loading was increased from C5-MO to C20-MO.

Due to the atomic selectivity, the monitoring of thermal decomposition by quick-EXAFS spectroscopy provides insights into the phase transformation of each 3d cation, with no interference due to signal overlap (unlike XRD). Furthermore, the technique reveals the full composition of the sample, regardless of the existence of long-range order. For the zinc-phase speciation, it was expected that the Zn-LDH species were transformed into a mixture of nano-ZnO and nano-$ZnAl_2O_4$ species.[39] In a first analysis of the quick-XAS data recorded during the LDH thermal decomposition, the MCR-ALS minimization, considering only three components, gave acceptable residual factors, R_f, regarding the reconstruction of the spectra (Figure S4), but with $ZnAl_2O_4$ concentrations above those permitted (Figure S5) considering the LDH stoichiometry. At temperatures above 120-150 °C, there was a slight increase of the R_f factors calculated using 3 components, which was significant due to the lack of noise. The not entirely consistent $ZnAl_2O_4$ proportion obtained with 3 components, together with the non-random deviation of R_f factors, compared to the lack-of-fit (LOF) parameter, suggested that the rank of the matrix used for the MCR-ALS minimization of the thermal decomposition dataset was underestimated. This issue can occur when there is extensive similarity among species spectra or co-evolution of concentration

profiles.[40] In order to overcome the rank deficiency issue and isolate the spectra of the pure components, all the Zn spectra measured at RT after thermal decomposition and with different LDH compositions[41] were analyzed together. Also included were some RT spectra measured after the thermal decomposition of a ZnAl-LDH with Zn:Al molar ratio of 0.5:1 (stoichiometry favoring $ZnAl_2O_4$ formation), together with some Zn K-edge XAS spectra of a CuZnAl-PMMA nanocomposite calcined in a static atmosphere. This enabled construction of a spectral dataset known as a column-wise augmented (CWA) dataset, with wide and important variations in composition and process parameters. It was then possible to extract the expected ZnO and $ZnAl_2O_4$ components, identified by comparison of their XANES spectra with those of ZnO and $ZnAl_2O_4$ references,[23, 39] together with a fourth component.

The XANES spectra and Fourier transforms (FT) of these components are presented in Figure 3. For the ZnO and $ZnAl_2O_4$ species isolated by MCR-ALS, the second coordination shell (second contribution at around 0.30 nm after FT) showed significant differences in intensity, compared to the crystalline reference signals (Figure 3b and 3c). This feature was related to the nanometric size of the phases isolated by MCR-ALS, in agreement with the XRD results, showing the presence of a poorly crystalline ZnO phase and the absence of diffraction signals related to the nano-$ZnAl_2O_4$ phase. The FT analysis of the quick-EXAFS spectrum of the fourth component (Figure 3d) revealed a four-fold coordination for the Zn absorbing atom, with a first coordination shell of 3.9 ± 0.2 oxygen atoms at 0.192 ± 0.001 nm. The shape of the XANES spectrum isolated for this fourth component was consistent with the formation of a tetrahedral Zn species, as encountered for products of Zn(II) sorption on metal (hydr)oxides.[42, 43] This species, hereafter called tetrahedral Zn pre-nucleus (TPN), was assumed to be formed during the early stage of the dehydroxylation process, by the departure of Zn atoms embedded in the LDH layers. The

tetrahedral Zn(II) species could still be in corner-sharing interaction with the LDH layer, as described for complexes sorbed on alumina or ferrihydrite powders.[42, 43] In the latter case, defined structures are proposed, with Al or Fe atoms coordinated to Zn as second neighbors. Here, the intensity of the contribution of the second nearest neighbors was very low, compared to the nano-ZnO and nano-$ZnAl_2O_4$, precluding EXAFS fitting and suggesting various coordinations of the Zn tetrahedrons to the lamellae. It is noteworthy that the presence of this component was essential to explain the experimental data variance, respecting the $ZnAl_2O_4$ concentration constraint.

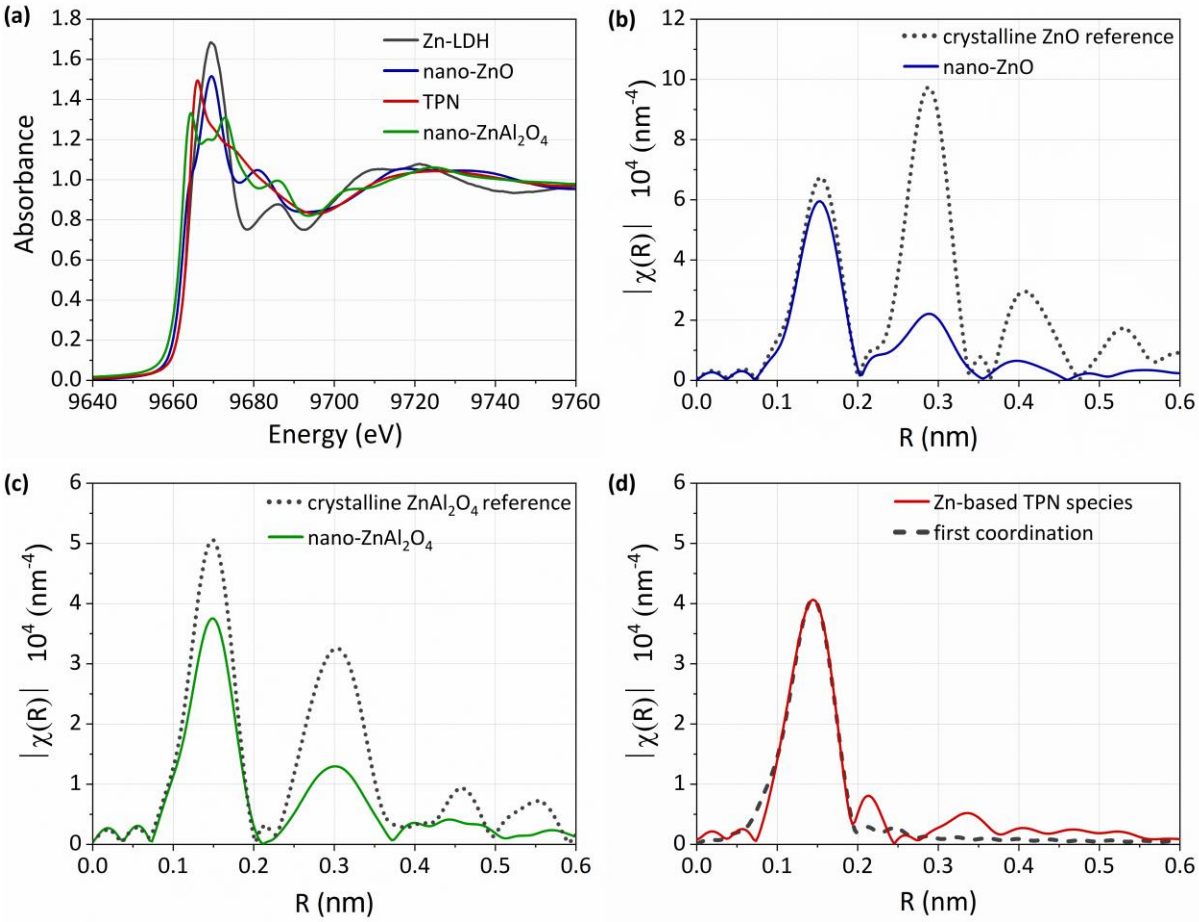

Figure 3. (a) XANES spectra obtained from the MCR-ALS analysis of the Zn-based species, and FT of the EXAFS spectra isolated by MCR-ALS of (b) nano-ZnO, (c) nano-$ZnAl_2O_4$, and (d) TPN species, in R space, compared to the crystalline ZnO and $ZnAl_2O_4$ references. The dashed line in (d) corresponds to fitting of the TPN first coordination shell.

Considering this information, the zinc spectra datasets (Figure S6) were minimized by MCR-ALS, using the four isolated spectra (Figure 3a). The R_f factors did not deviate from the LOF value obtained for the minimization with 4 components (Fig S4), indicating the reliability of the MCR-ALS solution so-obtained.

The concentration profiles obtained by MCR-ALS are shown in Figure 4 for all the zinc and copper species involved in the LDH thermal decomposition. During the thermal decomposition (Figure S7a), the Cu-LDH species were directly transformed into a nano-

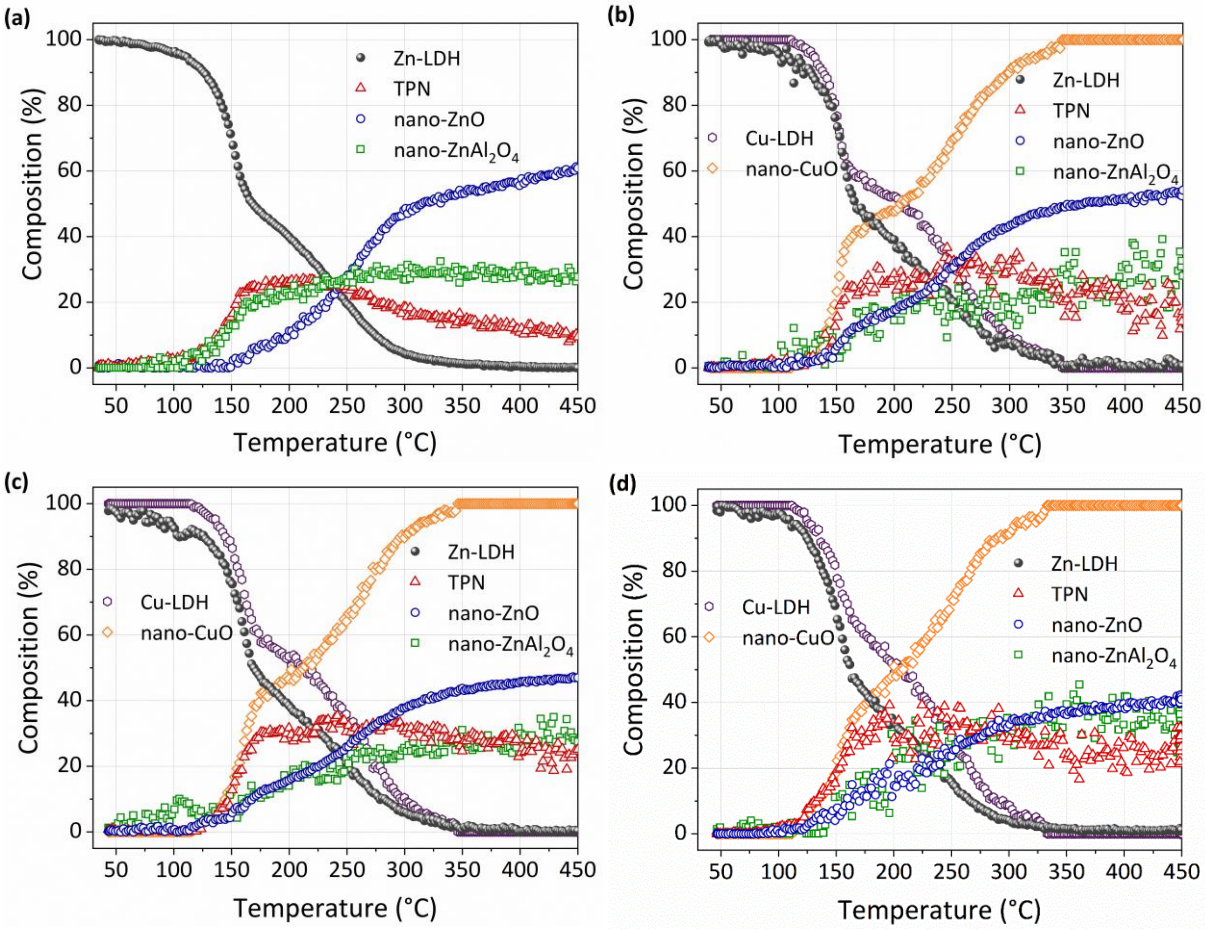

Figure 4. Concentration profiles of Cu and Zn-based species during thermal decomposition of (a) C0-LDH, (b) C5-LDH, (c) C10-LDH, and (d) C20-LDH, from MCR-ALS analysis of the Cu and Zn K-edge data. For the latter, minimization was carried out according to the CWA strategy, resulting in consideration of 4 components for the MCR-ALS analysis.

CuO species (Figure S7b and S7c) at temperatures higher than 120 °C, reaching 100% at approximately 350 °C, irrespective of the Cu content (Figure 4). In agreement with the TGA and DSC results (Figure 1), the LDH decomposition proceeded according to a two-step process for all the samples, with a first fast conversion of ~40-50% at around 150 °C, followed by a slower event between 150 and 350 °C. The same formation dynamics of nano-CuO were observed for the CuZnAl LDH samples. In particular, the derivatives of the nano-CuO percentage profile, presented in Figure S8, displayed a similar shape as the heat flow patterns derived from DSC analysis (Figure 1). It is also important to highlight the correlation between the first step of nano-CuO formation with the formation of TPN and the second ones with the formation of nano-$ZnAl_2O_4$ and nano-ZnO, both co-evolving up to 250 °C.

For the C0-LDH sample, the onsets of formation of the TPN and nano-$ZnAl_2O_4$ species were concomitant and with the same conversion rate between 120 and 150 °C (Figure 4a). When the TPN and nano-$ZnAl_2O_4$ were near the steady-state composition (at ~150 °C), the onset of formation of nano-ZnO started from the C0-LDH conversion, while above 250 °C, it was fed by the end of LDH conversion and by TPN accretion. This behavior indicated that dehydroxylation of the LDH lamellae first occurred around Al-rich sites of the ZnAl-LDH sheet.

When Zn was isomorphically substituted by Cu, the clear separation of TPN formation from the nano-$ZnAl_2O_4$ and nano-ZnO species indicated that the structural distortions in the layered LDH network, associated with the Jahn-Teller effect for octahedral Cu species, induced the formation of sites that were energetically more favorable for early dehydroxylation than the Al sites.[36, 37, 39] This was responsible for the early exit of copper from the sheet, compared to the trivalent cations in C0-LDH, favoring the concomitant TPN formation.[39] As a matter of fact, it was evident that the

higher the loading of Cu in the sample, the lower the onset temperature for CuO formation (Figure S8).

The compositions of the mixed oxides after the thermal decomposition are summarized in Figure 5, evidencing that a higher Cu content led to increase the amounts of TPN and nano-$ZnAl_2O_4$ species, while the nano-ZnO species decreased. After the LDH thermal decompositions, comparison was made of the FT of the Cu K-edge EXAFS spectra measured at RT (Figure S7c). The EXAFS fitting (Figure S9, Table S1) revealed a Jahn-Teller arrangement for the oxygen coordination shell, with 4 atoms at 0.196 nm and 2 atoms at 0.29-0.30 nm, as encountered for CuO,[44] and a Cu-Cu contribution at 0.341-0.344 nm, indicating the formation of a copper oxide-like structure, but with much smaller nanoparticle sizes, compared to the crystalline CuO reference.

3.3. Catalyst activation: genesis of the metallic nanoparticles

The reducibility of the MO samples was evaluated by temperature-programmed reduction (TPR)

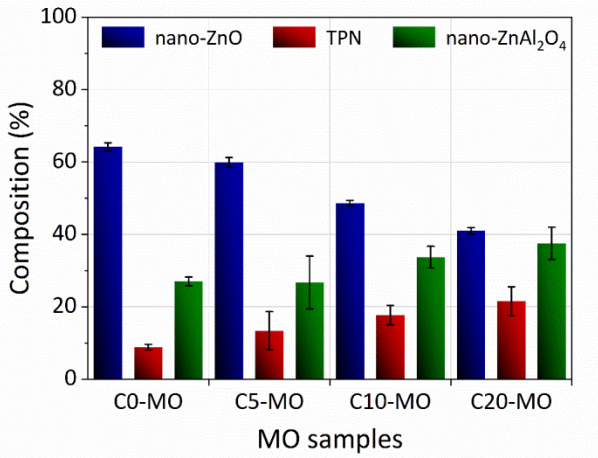

Figure 5. Zn-based species percentages for the MO samples obtained after thermal decomposition of the LDH samples, measured at RT. These percentages were determined by MCR-ALS analysis.

XAS measurements from RT to 500 °C, under an atmosphere of 5% H_2/95% He. The results indicated that the Cu^{2+} species were reduced in two steps (Cu^{2+} to Cu^{+}, followed by Cu^{+} to Cu^{0}), as reported elsewhere.[21, 45] The Cu K-edge XAS spectra datasets (Figure S10a) were minimized by MCR-ALS, using 3 components identified by their XANES and EXAFS fingerprints (Figure S10) as the starting nano-CuO, nano-Cu_2O (Figure S11, Tables S1 and S2), and nano-Cu^0 species. For all samples, the temperature evolutions of the Cu-based species (Figure S12) showed the Cu^{2+}/Cu^{+} transformation at around 240 °C. On the other hand, the lower the copper content in the initial LDH, the greater the stability of the Cu^{+} species (up to 425 °C for C5-MO and up to 340 °C for C10-MO and C20-MO).

For the catalytic reaction, the catalysts were activated at 350 °C for 15 min, under a 30 mL min^{-1} flow of 5% H_2/95% He (Figure 6). Similar to the behavior observed during the TPR-XAS experiments, the lower the copper content, the greater the Cu^{+} stability, with the time required for complete Cu reduction increasing from 6 to 9 min as the amount of copper in the LDH decreased from 20 to 5 wt.%. This provided clear evidence of the higher kinetic stability of the well-dispersed monovalent copper species, due to the greater diffusional distances between the nano-Cu_2O species on the support surface.[4]

The kinetic stability of the nano-Cu^0 dispersed phase was analyzed quantitatively using the Johnson-Mehl-Avrami (JMA) first order phase transition model, considering isothermally conducted solid-state phase transformations.[46] The continuous lines in Figure 6 show the quality of the fits of the nano-Cu^0 species evolution obtained by the JMA equation for the transformed fraction (X (t)), as a function of time (t):[46, 47]

$$X(t) = 1 - \exp\left(\frac{C}{n}\,\Gamma\,\gamma^{n-1}\,t^{n}\right) \quad (8)$$

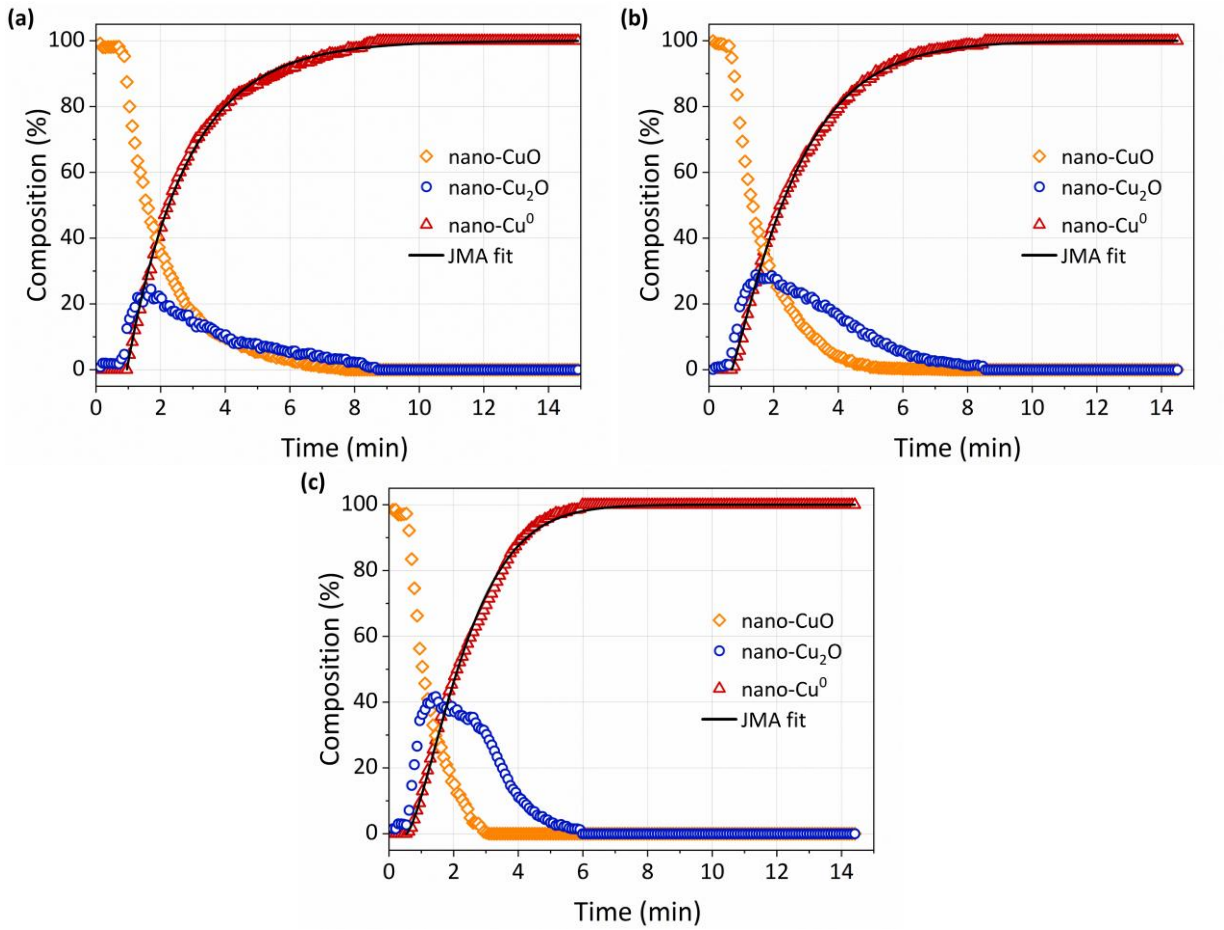

Figure 6. MCR-ALS deriver evolution of copper species composition during isothermal activation at 350 °C for the catalysts (a) C5, (b) C10, and (c) C20, obtained from quick-XAS measurements. The continuous lines represent the fits of nano-Cu0 evolution using the JMA model.

where, C has values of 1, 2, π, and 4π/3 for dimensionalities (d = n-1) of 0, 1, 2, and 3, respectively, n is the dynamic exponent, and Γ and γ are the nucleation and growth rates. The n values obtained were close to 1 for all samples (Table S3), indicating that the formation of metallic copper was restricted to the nucleation step, generating infinitesimal (point-like) metallic particles at the catalyst surface.[48] It should also be noted that as the copper loading increased, the values of n were minimally deviated from 1, suggesting slight growth of the particles. Independent evidence of the

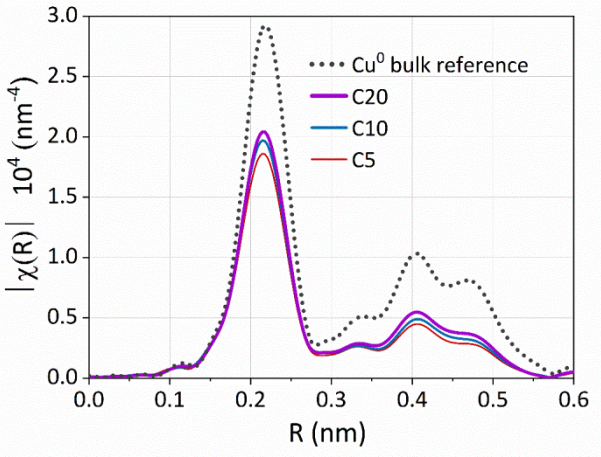

Figure 7. Fourier transforms of the EXAFS spectra obtained at 55 °C for the activated catalysts with different Cu loadings, compared to the metallic Cu reference.

kinetic stability of the well-dispersed nano-Cu^0 particles was provided by the EXAFS and HAADF-STEM analyses.

The Fourier transforms of the EXAFS signals for the activated samples (Figure 7) were analyzed to obtain the first nearest neighbor coordination numbers (N_{Cu-Cu}) and their distances (R_{Cu-Cu}). The lower intensities of the first and second coordination shells,

Table 1. Structural parameters of copper nanoclusters, calculated from the EXAFS fitting[(a)] for the catalysts with different Cu loadings, measured at 55 °C.

Sample	N_{Cu-Cu}[(a)]	R_{Cu-Cu}[(a,b)] (nm)	L[(c)]	d_{Cu}[(c)] (nm)	S_{Cu}[(c)] ($m^2\ g_{cat}^{-1}$)	D_{Cu}[(c)] (%)
Ref.	12.0	0.255	-	-	-	-
C5	10.0 ± 0.17	0.254	4.9	2.3 ± 0.15	15 ± 1.0	46 ± 3.1
C10	10.6 ± 0.14	0.254	7.1	3.0 ± 0.27	22 ± 1.9	34 ± 3.0
C20	10.7 ± 0.17	0.254	8.0	3.4 ± 0.38	40 ± 4.6	31 ± 3.5

[(a)] $S_0^2 = 0.915$ determined from the Cu^0 bulk reference and $\sigma^2 = 0.00011\ nm^2$ fixed for all samples. [(b)]Radial distance errors were 0.004, 0.004, and 0.003 nm for C5, C10, and C20, respectively. [(c)]Assuming a cuboctahedral model.

compared to the bulk Cu^0 reference, were related to the number of copper atoms present in the metallic clusters[34] (L) and, consequently, to their size (d_{Cu}), copper surface area (S_{Cu}), and copper dispersion (D_{Cu}). Table 1 summarizes the results for these parameters derived from the EXAFS coordination numbers using Equations (4) to (7). The metallic cluster size, d_{Cu}, increased with the copper content (C5 < C10 < C20), consequently decreasing the apparent Cu^0 dispersion, D_{Cu}. However, the metallic area per gram of catalyst, S_{Cu}, increased as a consequence of the increased number of clusters (higher copper loadings), whereas the metallic area of the catalyst per gram of copper decreased from 296 ± 20 to 202 ± 23 $m^2\ g_{Cu}^{-1}$ when the copper loading increased from 5 to 20% (with 223 ± 19 $m^2\ g_{Cu}^{-1}$ for the C10 sample).

The crystalline structures and morphologies of the activated samples were analyzed by XRD and TEM, respectively. The HAADF-STEM images (Figure 8) showed that the supported catalyst retained the platelet-like morphology characteristic of the calcined LDH structures,[19] with metallic copper nanoparticles smaller than 10 nm randomly distributed on the platelets (Figure 8a). The chemical mapping by EDX confirmed the high dispersion of copper on the platelet surface

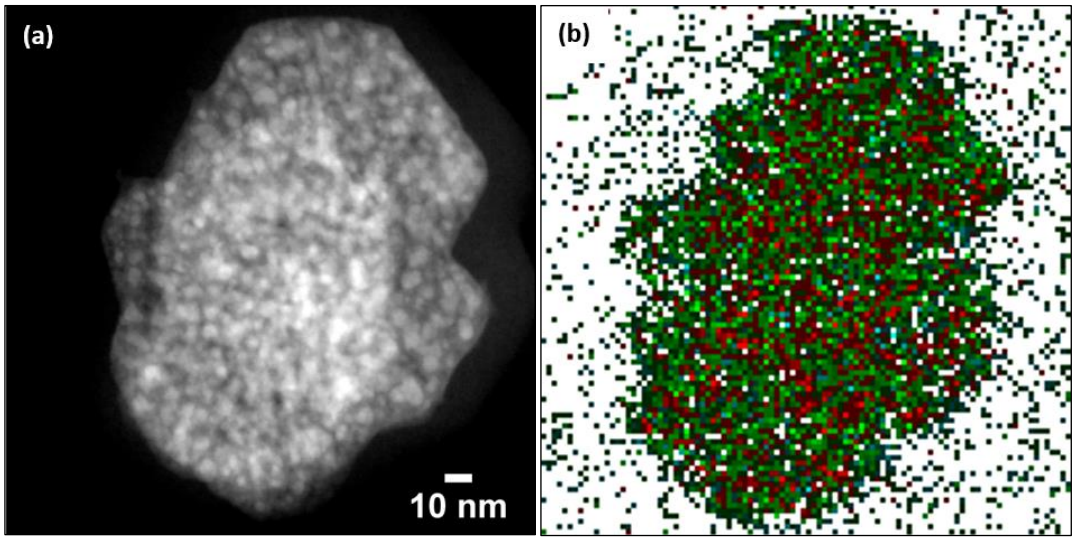

Figure 8. (a) HAADF-STEM image of the activated C20 catalyst, and (b) EDX chemical mapping of the same region for aluminum (blue), zinc (green), and copper (red).

(Figure 8b). The X-ray diffractograms (Figure S13) showed the appearance of the (111), (200), and (220) peaks related to the Cu^0 structure. The crystallite sizes, calculated using the Scherrer equation, were 2.4, 3.0, and 4.1 nm for the activated C5-MO, C10-MO, and C20-MO, respectively, in agreement with the Cu^0 nanoparticle sizes obtained by EXAFS (Table 1) and also confirmed by the TEM micrographs, from which the average particle sizes were 2.8, 3.1, and 3.5 nm (Figure S14).

A notable feature was the correlation between the proportion of ZnO composing the MO samples and the Cu^0 dispersion after activation, with a higher nano-ZnO percentage (Figure 5) being associated with greater Cu^0 dispersion (Table 1). This could be attributed to the physical spacing provided by the nano-ZnO, with strong Cu-ZnO interfacial contacts hindering Cu nanoparticle sintering. Therefore, the preparation route based on LDH decomposition, leading to metal oxide particles with nanometric sizes, appeared to be essential for stabilizing Cu particles against sintering.[12, 49]

3.4. Catalytic properties

After catalyst activation, the copper nanoparticles remained unchanged, as nano-Cu^0 species, throughout the EDR at different temperatures. Likewise, the relative proportions of the zinc-based species obtained after the LDH thermal decompositions remained almost unchanged during the activation step and the EDR (Figure S15).

Figure 9 shows the effect of the Cu loading on ethanol conversion, as a function of the reaction temperature (220, 250, 300, and 350 °C). On the one hand, for all temperatures, there was a nonlinear increase in ethanol conversion (χ_{EtOH}), as the Cu loading was increased. On the other hand, with increasing temperature, an almost linear increase in ethanol conversion was observed

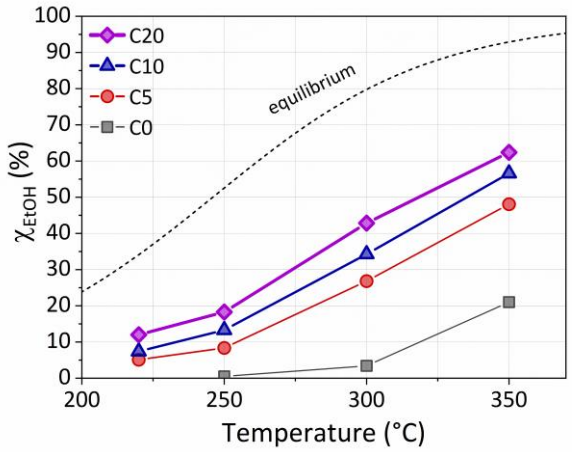

Figure 9. Ethanol conversion in the EDR at different temperatures, using catalysts with different Cu loadings.

for all the copper catalysts (Table 2). The main reaction product was acetaldehyde, with selectivity (S_{AcH}) above 97.4% for all the copper catalysts. Byproducts of ethanol transformation were also formed at low concentrations (S_{others}), including ethyl acetate, acetone, and diethyl ether (Figure 10). The catalytic test was also performed using the C0 sample, for which no substantial conversion was observed, compared to the copper-loaded samples. This confirmed that the adsorption occurred on the copper sites. In agreement with the values of the metallic areas of the catalysts per gram of copper, the turnover frequency (TOF) measured at a given temperature decreased with increase of the copper content. However, a higher copper content led to greater acetaldehyde production (higher activity), since the ethanol conversion increased, while the selectivity towards acetaldehyde remained almost constant. In addition, for a given composition, the TOF increased with the temperature. It is noteworthy that for conventional catalysts prepared from Cu/ZnO or Cu/ZnO/Al_2O_3, the selectivity to acetaldehyde usually decreases with increase of the temperature,[11, 50] whereas the selectivity reported for the Cu/$ZnAl_2O_4$ catalytic system[1] remains high and constant at temperatures up to 500 °C. The high selectivity to acetaldehyde observed

here, when the temperature was increased from 300 to 350 °C, could be attributed to the multiple components in the support derived from the LDH thermal decomposition, especially the presence of nano-$ZnAl_2O_4$. Therefore, the co-evolution of the relative proportion of nano-$ZnAl_2O_4$ with the copper loading (Figure 5) could have a positive impact on the selectivity to acetaldehyde for conversion at high temperature.

Table 2. Dehydrogenation activities, at different temperatures, for the activated catalysts with different Cu loadings.

Sample	T. (°C)	χ_{EtOH} (%)	S_{AcH} (%)	Activity[(a)] ($mmol_{AcH}\ g^{-1}\ h^{-1}$)	TOF · 10^{-1} (s^{-1})
C0-MO	250	0.51	81	4.2	-
	300	3.3	94	32	-
	350	20	96	197	-
C5-MO	220	5.1	99	52	0.40
	250	8.2	97	82	0.65
	300	27	98	272	2.1
	350	48	96	474	3.8
C10-MO	220	7.4	99	75	0.39
	250	13	99	132	0.69
	300	34	98	343	1.8
	350	57	97	568	3.0
C20-MO	220	12	99	126	0.36
	250	18	99	183	0.53
	300	43	99	438	1.2
	350	63	97	618	1.8

[(a)] Activity towards AcH $= \frac{S_{AcH} \cdot \text{molar flow of converted ethanol}}{catalyst\ mass}$.

Regardless of the copper content, the catalysts showed excellent stability for 6 h on-stream at 300 and 350 °C, with no significant deactivation (Figure 10). In order to highlight the influence of the preparation route of the catalyst oxidic precursors on the catalytic performance, evaluations were also made of a 20 wt.% Cu-impregnated C0-LDH (IMP-LDH) and ZnO/Al_2O_3 (IMP-REF) samples with specific surface areas of 59 and 2 $m^2\ g^{-1}$. The chemical compositions of these samples were close to that of C20, but it was composed of larger CuO and ZnO crystallites, as evidenced by comparison of the Fourier transforms of the Zn and Cu K-edges EXAFS signals recorded after calcination of both samples (C20-MO and IMP-REF) in air (Figure S16). The JMA modeling of the isothermal activation of the IMP-REF catalyst at 350 °C, under 5% H_2/95% He, revealed an Avrami exponent (n) of 4 (Figure S17), in agreement with 3D growth of Cu^0 nanoparticles and highlighting very different nucleation and growth patterns, compared to those obtained for activation of the Cu-LDH-based precursors. The overall consequence was the

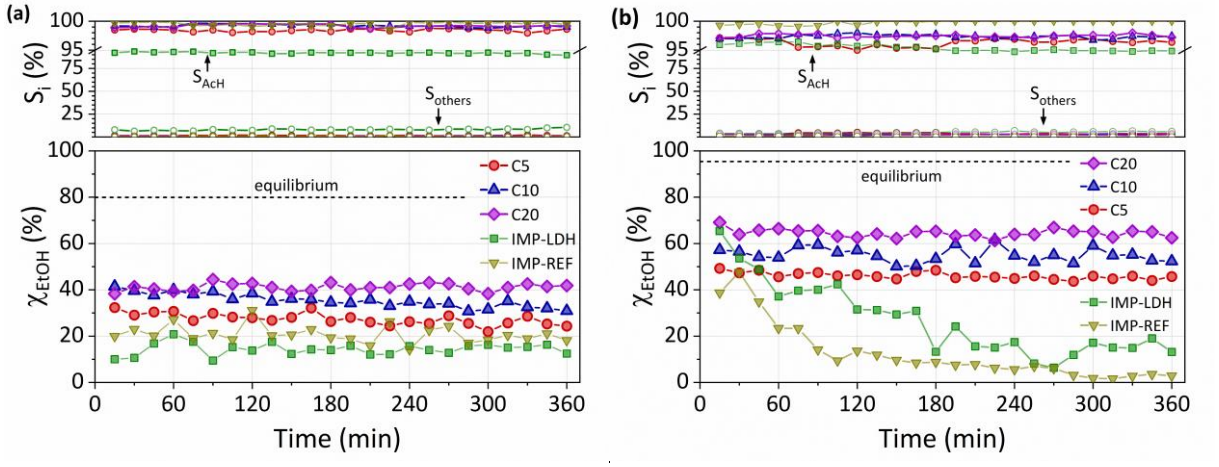

Figure 10. Ethanol conversion and selectivity in the EDR at (a) 300 °C and (b) 350 °C, during 6 h on-stream, for catalysts with different Cu loadings. The green and yellow lines refer to the reference samples (IMP-LDH and IMP-REF) prepared by impregnation of C0-LDH and commercial ZnO/Al_2O_3, respectively, with 20 wt.% Cu.

formation of larger Cu^0 nanoparticles for the impregnated catalysts, compared to the LDH-derived catalysts. Despite good stability at 300 °C, the impregnated catalysts provided low conversions of around half that observed for C20-MO, while being rapidly deactivated in less than 2 h of reaction at 350 °C (Figure 10). In addition to the low Cu dispersion associated with the formation of large Cu crystallites, which explained the lower conversion than for the LDH-derived catalysts, the weaker metal-support interactions associated with the presence of large ZnO crystallites (Figure S16) allowed the migration of copper on the catalyst surface,[12] leading to deactivation by sintering, as evidenced by the XRD results (Figure S18).

In the present LDH-derived system, the role of the nano-ZnO support in stabilization of the active phase dispersion seemed to prevent this harmful effect, allowing the catalysts to remain active for a longer time. An essential feature of the LDH-derived catalysts was that the calcined material retained the same platelet shape as the precursor, forming paracrystalline oxide phases.[51] Furthermore, the copper species were already homogeneously dispersed on the pristine LDH and over the derived mixed nano-oxide support,[18] favoring greater nanocrystallinity and stability of the metallic copper catalyst, compared to most catalysts prepared using conventional impregnation methods.

4. CONCLUSIONS

Copper-based catalysts derived from CuZnAl-LDH were successfully prepared with different copper loadings (5, 10, and 20 wt.%). The *in situ* quick-EXAFS investigations of all the Zn and Cu species, together with the multivariate MCR-ALS analysis, showed that the copper loading affected the Zn-based species composition of the supported catalysts. The lower the Cu loading, the higher the nano-ZnO content, decreasing the nano-$ZnAl_2O_4$ and zinc tetrahedral pre-nuclei

(TPN) contents in the final catalyst. Furthermore, higher copper dispersions were observed with lower copper loadings and higher nano-ZnO contents.

The catalysts were very active for the ethanol dehydrogenation reaction, with conversions of up to 43% at 300 °C and 63% at 350 °C. All the samples showed high selectivity towards acetaldehyde (>97%) and stability in the reaction at 300 °C, with no deactivation during 6 h on-stream. Although the samples with lower copper contents presented higher dispersions and reactivities, the sample containing 20 wt.% of copper outperformed the others, with higher conversion and activity towards acetaldehyde.

Finally, the results highlighted the importance of the synthesis method used to prepare supported metal catalysts, for fine tuning of the phase dispersion and control of catalyst selectivity and stability. The $Cu/ZnO/ZnAl_2O_4$ catalysts prepared using the LDH precursor route could be very efficient in many other important catalytic reactions, such as the synthesis of methanol from CO_2.[12, 52]

ASSOCIATED CONTENTS

XRD data, N_2 adsorption-desorption isotherms, SEM, XAS spectra datasets and analyses, MCR-ALS results, EXAFS spectra and fittings, TPR-XANES, HAADF-STEM micrographs (PDF)

AUTHOR INFORMATION

Corresponding Authors

Rodrigo M. M. Santos - São Paulo State University (UNESP), Institute of Chemistry, Rua Prof. Francisco Degni 55, 14800-060, Araraquara, SP, Brazil; SOLEIL Synchrotron, L'Orme des

Merisiers, BP48, Saint-Aubin, 91192, Gif-sur-Yvette, France; orcid.org/0000-0002-8761-6240; Email: rodrigo.morais@unesp.br

Celso V. Santilli - São Paulo State University (UNESP), Institute of Chemistry, Rua Prof. Francisco Degni 55, 14800-060, Araraquara, SP, Brazil; orcid.org/0000-0002-8356-8093; Email: cv.santilli@unesp.br

Authors

Valérie Briois – UR1-CNRS, SOLEIL Synchrotron, L'Orme des Merisiers, BP48, Saint-Aubin, 91192, Gif-sur-Yvette, France; orcid.org/0000-0002-8172-2755

Leandro Martins - São Paulo State University (UNESP), Institute of Chemistry, Rua Prof. Francisco Degni 55, 14800-060, Araraquara, SP, Brazil; orcid.org/0000-0003-2229-5316

Notes

The authors declare no competing financial interest.

Author Contributions

The manuscript was written through contributions of all authors. All authors have given approval to the final version of the manuscript.

ACKNOWLEDGEMENTS

The authors are grateful for the financial support received from the São Paulo State Research Foundation (FAPESP, grants 2015/23410-5, 2017/13821-3, and 2018/01258-5) and the National Council for Scientific and Technological Development (CNPq, grants 309419/2020-4 and 430758/2018-9). We also thank Synchrotron SOLEIL (France) for the quick-XAS experiments at the ROCK beamline, which was supported by a public grant overseen by the French National

Research Agency (ANR), as part of the *"Investissements d'Avenir"* program (reference: ANR-10-EQPX-45).

REFERENCES

1. Garbarino, G.; Riani, P.; Villa García, M.; Finocchio, E.; Sanchez Escribano, V.; Busca, G. A Study of Ethanol Dehydrogenation to Acetaldehyde over Copper/Zinc Aluminate Catalysts. *Catalysis Today* **2020,** *354*, 167-175.

2. *Acetaldehyde Market trends, Global Industry Analysts Inc., strategy.com/MarketResearch/Acetaldehyde-Ethanal-Market-Trends.asp.*

3. Luizon Filho, R. A.; Possato, L. G.; Santisteban, O. A. N.; de Vasconcellos, A.; da Silva, D. A.; Lima, M. F.; Martins, L.; Nery, J. G. Synthesis and Characterization of Chromium Silicate Catalyst and its Application in the Gas Phase Glycerol Transformation into Acetaldehyde. *Inorganic Chemistry Communications* **2020,** *112*, 107710.

4. Cassinelli, W. H.; Martins, L.; Passos, A. R.; Pulcinelli, S. H.; Rochet, A.; Briois, V.; Santilli, C. V. Correlation between Structural and Catalytic Properties of Copper Supported on Porous Alumina for the Ethanol Dehydrogenation Reaction. *ChemCatChem* **2015,** *7* (11), 1668-1677.

5. Sato, A. G.; Volanti, D. P.; Meira, D. M.; Damyanova, S.; Longo, E.; Bueno, J. M. C. Effect of the ZrO_2 Phase on the Structure and Behavior of Supported Cu Catalysts for Ethanol Conversion. *Journal of Catalysis* **2013,** *307*, 1-17.

6. Santacesaria, E.; Carotenuto, G.; Tesser, R.; Di Serio, M. Ethanol Dehydrogenation to Ethyl Acetate by using Copper and Copper Chromite Catalysts. *Chemical Engineering Journal* **2012,** *179*, 209-220.

7. Inui, K.; Kurabayashi, T.; Sato, S.; Ichikawa, N. Effective Formation of Ethyl Acetate from Ethanol over Cu-Zn-Zr-Al-O Catalyst. *Journal of Molecular Catalysis A: Chemical* **2004,** *216* (1), 147-156.

8. Cassinelli, W. H.; Martins, L.; Magnani, M.; Pulcinelli, S. H.; Briois, V.; Santilli, C. V. Time-Resolved XAS/MS/Raman Monitoring of Mutual Copper Self-Reduction and Ethanol Dehydrogenation Reactions. *RSC Advances* **2016,** *6* (25), 20453-20457.

9. Argyle, M. D.; Bartholomew, C. H. Heterogeneous Catalyst Deactivation and Regeneration: A Review. *Catalysts* **2015,** *5* (1), 145-269.

10. De Waele, J.; Galvita, V. V.; Poelman, H.; Gabrovska, M.; Nikolova, D.; Damyanova, S.; Thybaut, J. W. Ethanol Dehydrogenation over Cu Catalysts Promoted with Ni: Stability Control. *Applied Catalysis A: General* **2020,** *591*, 117401.

11. Fujita, S.-i.; Iwasa, N.; Tani, H.; Nomura, W.; Arai, M.; Takezawa, N. Dehydrogenation of Ethanol Over Cu/ZnO Catalysts Prepared from Various Coprecipitated Precursors. *Reaction Kinetics and Catalysis Letters* **2001,** *73* (2), 367-372.

12. Natesakhawat, S.; Ohodnicki, P. R.; Howard, B. H.; Lekse, J. W.; Baltrus, J. P.; Matranga, C. Adsorption and Deactivation Characteristics of Cu/ZnO-Based Catalysts for Methanol Synthesis from Carbon Dioxide. *Topics in Catalysis* **2013,** *56* (18), 1752-1763.

13. Kurr, P.; Kasatkin, I.; Girgsdies, F.; Trunschke, A.; Schlögl, R.; Ressler, T. Microstructural Characterization of $Cu/ZnO/Al_2O_3$ Catalysts for Methanol Steam Reforming: A Comparative Study. *Applied Catalysis A: General* **2008,** *348* (2), 153-164.

14. Gaspar, A. B.; Barbosa, F. G.; Letichevsky, S.; Appel, L. G. The One-Pot Ethyl Acetate Syntheses: The Role of the Support in the Oxidative and the Dehydrogenative Routes. *Applied Catalysis A: General* **2010,** *380* (1), 113-117.

15. Santos, R. M. M.; Tronto, J.; Briois, V.; Santilli, C. V. Thermal Decomposition and Recovery Properties of $ZnAl\text{-}CO_3$ Layered Double Hydroxide for Anionic Dye Adsorption: Insight into the Aggregative Nucleation and Growth Mechanism of the LDH Memory Effect. *Journal of Materials Chemistry A* **2017,** *5* (20), 9998-10009.

16. Hibino, T. Anion Selectivity of Layered Double Hydroxides: Effects of Crystallinity and Charge Density. *European Journal of Inorganic Chemistry* **2018,** *2018* (6), 722-730.

17. Petrolini, D. D.; Cassinelli, W. H.; Pereira, C. A.; Urquieta-González, E. A.; Santilli, C. V.; Martins, L. Ethanol Dehydrogenative Reactions Catalyzed by Copper Supported on Porous Al–Mg Mixed Oxides. *RSC Advances* **2019,** *9*, 3294-3302.

18. Fan, G.; Li, F.; Evans, D. G.; Duan, X. Catalytic Applications of Layered Double Hydroxides: Recent Advances and Perspectives. *Chemical Society Reviews* **2014,** *43* (20), 7040-7066.

19. Hobbs, C.; Jaskaniec, S.; McCarthy, E. K.; Downing, C.; Opelt, K.; Güth, K.; Shmeliov, A.; Mourad, M. C. D.; Mandel, K.; Nicolosi, V. Structural Transformation of Layered Double Hydroxides: An in Situ TEM Analysis. *npj 2D Materials and Applications* **2018,** *2* (1), 4.

20. Cassinelli, W. H.; Martins, L.; Passos, A. R.; Pulcinelli, S. H.; Santilli, C. V.; Rochet, A.; Briois, V. Multivariate Curve Resolution Analysis Applied to Time-Resolved Synchrotron X-ray Absorption Spectroscopy Monitoring of the Activation of Copper Alumina Catalyst. *Catalysis Today* **2014,** *229*, 114-122.

21. Passos, A. R.; Pulcinelli, S. H.; Santilli, C. V.; Briois, V. Operando Monitoring of Metal Sites and Coke Evolution during Non-Oxidative and Oxidative Ethanol Steam Reforming over Ni and NiCu Ex-Hydrotalcite Catalysts. *Catalysis Today* **2019,** *336*, 122-130.

22. Passos, A. R.; La Fontaine, C.; Pulcinelli, S. H.; Santilli, C. V.; Briois, V. Quick-EXAFS and Raman Monitoring of Activation, Reaction and Deactivation of NiCu Catalysts obtained from Hydrotalcite-Like Precursors. *Physical Chemistry Chemical Physics* **2020,** *22*, 18835-18848.

23. Carvalho, H. W. P.; Leroux, F.; Briois, V.; Santilli, C. V.; Pulcinelli, S. H. Thermal Stability of PMMA–LDH Nanocomposites: Decoupling the Physical Barrier, Radical Trapping, and Charring Contributions using XAS/WAXS/Raman Time-Resolved Experiments. *RSC Advances* **2018,** *8*, 34670-34681.

24. Brunauer, S.; Emmett, P. H.; Teller, E. Adsorption of Gases in Multimolecular Layers. *Journal of the American Chemical Society* **1938,** *60* (2), 309-319.

25. Barrett, E. P.; Joyner, L. G.; Halenda, P. P. The Determination of Pore Volume and Area Distributions in Porous Substances. I. Computations from Nitrogen Isotherms. *Journal of the American Chemical Society* **1951,** *73* (1), 373-380.

26. Briois, V.; La Fontaine, C.; Belin, S.; Barthe, L.; Moreno, T.; Pinty, V.; Carey, A.; Girardot, R.; Fonda, E. ROCK: the New Quick-EXAFS Beamline at SOLEIL. *Journal of Physics: Conference Series* **2016,** *712* (1), 012149.

27. Lesage, C.; Devers, E.; Legens, C.; Fernandes, G.; Roudenko, O.; Briois, V. High Pressure Cell for Edge Jumping X-ray Absorption Spectroscopy: Applications to Industrial Liquid Sulfidation of Hydrotreatment Catalysts. *Catalysis Today* **2019,** *336*, 63-73.

28. Jaumot, J.; Gargallo, R.; de Juan, A.; Tauler, R. A Graphical User-Friendly Interface for MCR-ALS: a New Tool for Multivariate Curve Resolution in MATLAB. *Chemometrics and Intelligent Laboratory Systems* **2005,** *76* (1), 101-110.

29. Jaumot, J.; de Juan, A.; Tauler, R. MCR-ALS GUI 2.0: New Features and Applications. *Chemometrics and Intelligent Laboratory Systems* **2015,** *140*, 1-12.

30. Hong, J.; Marceau, E.; Khodakov, A. Y.; Gaberová, L.; Griboval-Constant, A.; Girardon, J.-S.; Fontaine, C. L.; Briois, V. Speciation of Ruthenium as a Reduction Promoter of Silica-Supported Co Catalysts: A Time-Resolved in Situ XAS Investigation. *ACS Catalysis* **2015,** *5* (2), 1273-1282.

31. Rochet, A.; Baubet, B.; Moizan, V.; Pichon, C.; Briois, V. Co-K and Mo-K Edges Quick-XAS Study of the Sulphidation Properties of Mo/Al_2O_3 and $CoMo/Al_2O_3$ Catalysts. *Comptes Rendus Chimie* **2016,** *19* (10), 1337-1351.

32. Martini, A.; Borfecchia, E. Spectral Decomposition of X-ray Absorption Spectroscopy Datasets: Methods and Applications. *Crystals* **2020,** *10* (8).

33. Ravel, B.; Newville, M. ATHENA, ARTEMIS, HEPHAESTUS: Data Analysis for X-ray Absorption Spectroscopy using IFEFFIT. *Journal of Synchrotron Radiation* **2005,** *12* (4), 537-541.

34. Frenkel, A. Solving the 3D Structure of Metal Nanoparticles. *Zeitschrift für Kristallographie - Crystalline Materials* **2007,** *222* (11/2007), 605-611.

35. Han, J.; Zeng, H.-Y.; Xu, S.; Chen, C.-R.; Liu, X.-J. Catalytic Properties of CuMgAlO Catalyst and Degradation Mechanism in CWPO of Methyl Orange. *Applied Catalysis A: General* **2016,** *527*, 72-80.

36. Jahn, H. A.; Teller, E.; Donnan, F. G. Stability of Polyatomic Molecules in Degenerate Electronic States - I Orbital Degeneracy. *Proceedings of the Royal Society of London. Series A - Mathematical and Physical Sciences* **1937,** *161* (905), 220-235.

37. Roussel, H.; Briois, V.; Elkaim, E.; de Roy, A.; Besse, J. P. Cationic Order and Structure of [Zn−Cr−Cl] and [Cu−Cr−Cl] Layered Double Hydroxides: A XRD and EXAFS Study. *The Journal of Physical Chemistry B* **2000,** *104* (25), 5915-5923.

38. Santilli, C. V.; Pulcinelli, S. H. Análise da Textura de Materiais Cerâmicos a partir das Isotermas de Adsorção de Gases. *Cerâmica* **1993,** *39*, 11-16.

39. Carvalho, H. W. P.; Pulcinelli, S. H.; Santilli, C. V.; Leroux, F.; Meneau, F.; Briois, V. XAS/WAXS Time-Resolved Phase Speciation of Chlorine LDH Thermal Transformation: Emerging Roles of Isovalent Metal Substitution. *Chemistry of Materials* **2013,** *25* (14), 2855-2867.

40. de Juan, A.; Tauler, R. Chemometrics Applied to Unravel Multicomponent Processes and Mixtures: Revisiting Latest Trends in Multivariate Resolution. *Analytica Chimica Acta* **2003,** *500* (1), 195-210.

41. Ruckebusch, C.; De Juan, A.; Duponchel, L.; Huvenne, J. P. Matrix Augmentation for Breaking Rank-Deficiency: A Case Study. *Chemometrics and Intelligent Laboratory Systems* **2006,** *80* (2), 209-214.

42. Trainor, T. P.; Brown, G. E.; Parks, G. A. Adsorption and Precipitation of Aqueous Zn(II) on Alumina Powders. *Journal of Colloid and Interface Science* **2000,** *231* (2), 359-372.

43. Waychunas, G. A.; Fuller, C. C.; Davis, J. A.; Rehr, J. J. Surface Complexation and Precipitate Geometry for Aqueous Zn(II) Sorption on Ferrihydrite: II. XANES Analysis and Simulation. *Geochimica et Cosmochimica Acta* **2003,** *67* (5), 1031-1043.

44. Greschner, M. J.; Chen, N.; Yao, Y. Pressure-Driven Suppression of the Jahn–Teller Effects and Structural Changes in Cupric Oxide. *Journal of Physics: Condensed Matter* **2015,** *28* (2), 025401.

45. Kim, J. Y.; Rodriguez, J. A.; Hanson, J. C.; Frenkel, A. I.; Lee, P. L. Reduction of CuO and Cu_2O with H_2: H Embedding and Kinetic Effects in the Formation of Suboxides. *Journal of the American Chemical Society* **2003,** *125* (35), 10684-10692.

46. Avrami, M. Kinetics of Phase Change. I General Theory. *The Journal of Chemical Physics* **1939,** *7* (12), 1103-1112.

47. Liu, F.; Sommer, F.; Bos, C.; Mittemeijer, E. J. Analysis of Solid State Phase Transformation Kinetics: Models and Recipes. *International Materials Reviews* **2007,** *52* (4), 193-212.

48. Passos, A. R.; Martins, L.; Pulcinelli, S. H.; Santilli, C. V.; Briois, V. Correlation of Sol–Gel Alumina-Supported Cobalt Catalyst Processing to Cobalt Speciation, Ethanol Steam Reforming Activity, and Stability. *ChemCatChem* **2017,** *9* (20), 3918-3929.

49. Arena, F.; Barbera, K.; Italiano, G.; Bonura, G.; Spadaro, L.; Frusteri, F. Synthesis, Characterization and Activity Pattern of Cu–ZnO/ZrO_2 Catalysts in the Hydrogenation of Carbon Dioxide to Methanol. *Journal of Catalysis* **2007,** *249* (2), 185-194.

50. Tayrabekova, S.; Mäki-Arvela, P.; Peurla, M.; Paturi, P.; Eränen, K.; Ergazieva, G. E.; Aho, A.; Murzin, D. Y.; Dossumov, K. Catalytic Dehydrogenation of Ethanol into Acetaldehyde and Isobutanol using Mono- and Multicomponent Copper Catalysts. *Comptes Rendus Chimie* **2018,** *21* (3), 194-209.

51. Starukh, G.; Rozovik, O.; Oranska, O. Organo/Zn-Al LDH Nanocomposites for Cationic Dye Removal from Aqueous Media. *Nanoscale Research Letters* **2016,** *11:228* (1), 1-10.

52. van den Berg, R.; Prieto, G.; Korpershoek, G.; van der Wal, L. I.; van Bunningen, A. J.; Lægsgaard-Jørgensen, S.; de Jongh, P. E.; de Jong, K. P. Structure Sensitivity of Cu and CuZn Catalysts Relevant to Industrial Methanol Synthesis. *Nature Communications* **2016,** *7* (1), 13057.

TABLE OF CONTENTS (TOC) GRAPHIC